International Journal of Engineering Science 82 (2014) 28–45

Contents lists available at ScienceDirect

International Journal of Engineering Science

journal homepage: www.elsevier.com/locate/ijengsci

On the stability of boundary-layer flows over rotating spheroids

A. Samad [a], S.J. Garrett [b,*]

[a] Department of Mathematics, University of Peshawar, Pakistan
[b] Department of Mathematics, University of Leicester, UK

ARTICLE INFO

Article history:
Received 11 April 2013
Accepted 22 April 2014

Keywords:
3D boundary-layer transition
Convective instabilities
Crossflow
Rotating spheroid
Prolate geometry
Oblate geometry

ABSTRACT

We study linear convective instabilities within of the boundary-layer flows over spheroids rotating in otherwise still fluids. Particular spheroids within the prolate and oblate families are considered, each characterized by an eccentricity parameter, $0 \leqslant e \leqslant 0.7$. Viscous and streamline-curvature effects are included and local analyses conducted at latitudes between 10°–70° from the axis of rotation. Both travelling and stationary convective modes of type I (crossflow) and type II (streamline curvature) are found at each latitude within specific parameter spaces. The results of existing rotating-sphere investigations are reproduced at all latitudes in the limit of zero eccentricity.

In the prolate case, eccentricity is found to have a stabilizing effect on the type I mode at all latitudes and a destabilizing effect on the type II mode at latitudes above 50°. Eccentricity is therefore seen to be a destabilizing influence for low rotation rates (where instability occurs at high latitudes only and the type II mode dominates) and a stabilizing effect for high rotation rates (where instability occurs closer to the pole and the type I mode dominates). This effect is associated with the behavior of the local curvature of the prolate geometry as a function of eccentricity. In the oblate case, eccentricity is found to be universally stabilizing to both mode types at all latitudes. The oblate results demonstrate considerably lower sensitivity to eccentricity than the prolate results.

The most amplified modes are found to travel at 75% of the surface speed at each latitude and eccentricity for both spheroid families. This is consistent with existing theoretical studies of boundary-layer flows over the related geometries of the rotating-disk, -sphere and -cone, and leads to the prediction of *slow* vortices over highly-polished bodies.

1. Introduction

The boundary-layer flow over a rotating disk has served as the foremost model problem for studying transition in fully 3D incompressible boundary layers for over six decades, and has a huge body of associated literature (see (Gregory, Stuart, & Walker, 1955; Hussain, Garrett, & Stephen, 2011; Lingwood, 1995; Malik, 1986; Owen & Rogers, 1989; Reed & Saric, 1989; Saric, Reed, & White, 2003; Smith, 1947; Theodorsen & Regier, 1945; Wimmer, 1988), for example). The rotating-disk flow is of particular interest because it shares many similarities with the flow over swept wings (Reed & Saric, 1989; Saric et al., 2003; Wimmer, 1988) and types of rotating machinery (Hussain, Garrett, et al., 2011; Owen & Rogers, 1989) where laminar-turbulent transition is of significance in engineering design. However, continuing developments in spinning

* Corresponding author. Tel.: +44 0116 2523899.
E-mail addresses: mathematics.peshawar@gmail.com (A. Samad), sjg50@le.ac.uk (S.J. Garrett).

http://dx.doi.org/10.1016/j.ijengsci.2014.04.015
0020-7225/

projectiles, aerofoils and aeroengines has led to a need to understand the onset of laminar-turbulent transition of the boundary-layer flows over rotating cones and spheroids as objects in their own right.

Numerous flow-visualization studies, led by Kohama and Kobayashi, have been published (Kobayashi & Arai, 1990; Kobayashi, Kohama, & Kurosawa, 1983; Kobayashi & Izumi, 1983; Kohama, 1985; Kohama, 2000; Kohama & Kobayashi, 1983; Taniguchi, Kobayashi, & Fukunishi, 1998) which demonstrate an apparent similarity between the properties of rotating-disk, -cone and -sphere flows, as can seen in Fig. 1. In particular, it is clear that as one moves away from the pole within each geometry the flow is first laminar, with co-rotating spiral vortices appearing before their ultimate breakdown and the onset of the turbulent region; increasing the rotation rate of each body acts to move the transitional region closer to the pole. However, geometries other than the disk had received little analytical attention prior to 2002 when Garrett & co-workers commenced a series of studies of the boundary-layer flow over rotating cones and spheres (Barrow & Garrett, 2013; Garrett, 2002; Garrett & Peake, 2002, 2004, 2007; Garrett, Hussain, & Stephen, 2009; Garrett, Hussain, & Stephen, 2010; Garrett, 2010a, 2010b, 2010c; Hussain, Garrett, et al., 2011; Hussain, Stephen, & Garrett, 2011).

This present study should be considered as a generalization of Garrett's previous work on the stability of rotating-sphere flows to the two families (prolate and oblate) of rotating spheroids. Spheroids represent more practically significant rotating nose cones, and this is our motivation. We will see that the laminar flow and stability characteristics of the rotating-spheroid flow are closely related to the rotating-sphere flow. Indeed the sphere is a particular case of either spheroid type with zero cross-sectional eccentricity, and all are related to the rotating-disk flow in the region close to the pole. With this in mind, it is instructive to begin this study with a review of the existing work on the boundary-layer flow over the rotating sphere.

Theoretical studies of the stability of the rotating-sphere flow have been performed by Taniguchi et al. (1998), Garrett and Peake (2002, 2004), Barrow and Garrett (2013), who present local convective and absolute instability analyses of the boundary-layer flow for the sphere rotating both in and out of enforced axial flows and with and without surface mass flux. The studies focused on the calculation of the critical Reynolds numbers and other observable parameters at the onset of instabilities at each latitude. The stability analyses were a natural extension of the previous theoretical work into the steady flow profiles within the boundary layer (Banks, 1965; Banks, 1976; Manohar, 1967) and the stability analyses of the rotating-disk flow due to, for example, Malik (1986), Lingwood (1995). Garrett & Peake and Barrow & Garrett found that local convective-instability analyses could be used successfully to predict experimental observations (Kobayashi & Arai, 1990; Kohama & Kobayashi, 1983; Sawatzki, 1970) of the onset of spiral vortices at each latitude; furthermore, the onset of absolute instability appears to be related to the onset of turbulence (at least for low to moderate latitudes) and this is currently being explored further. As with rotating disks and broad cones, modes of type I (crossflow) and II (streamline curvature) were found to dictate the convective instability at all latitudes over the rotating sphere, and modes of type I and III, the absolute instability. Further information on these instability modes within the related boundary-layer flows can be found in Lingwood (1995), Garrett (2002), Garrett and Peake (2002, 2004, 2007), Garrett et al. (2009, 2010), Garrett (2010a, 2010b, 2010c), Hussain, Garrett, et al. (2011), Hussain, Stephen, et al. (2011) and Garrett (2011).

An interesting experimental observation made by Kobayashi and Arai (1990) was that the co-rotating spiral vortices were fixed on the sphere surface when the rotation rate was large (and transition occurred at low to moderate latitudes), whilst they moved relative to the sphere surface when the rotation rate was smaller (and transition occurred at high latitudes). The relative speed of the slow vortices was always around 76% of the local surface speed of the sphere. This observation was unique to this set of experiments, i.e. slow vortices had not been observed by Sawatzki (1970) or Kohama and Kobayashi (1983) and had not been observed in rotating-disk and cone experiments (see (Kobayashi et al., 1983; Kobayashi & Izumi, 1983; Kohama, 1985), for example). Garrett & Peake originally attempted to clarify the appearance of slow vortices using a method of investigation since denoted *method 1* in Garrett (2010a). This method involves calculating the critical parameters of a set of neutral curves, each pertaining to a different fixed azimuthal wavenumber of disturbance; the azimuthal phase velocity of disturbances, c, is then calculated from the globally-critical parameters and associated with the vortex speed. This approach predicted stationary vortices ($c = 1$) at all latitudes below 66°, where the type I mode dominates. Above this latitude an apparent point of inflection (rather than a global minimum) was found in the distribution of critical Reynolds

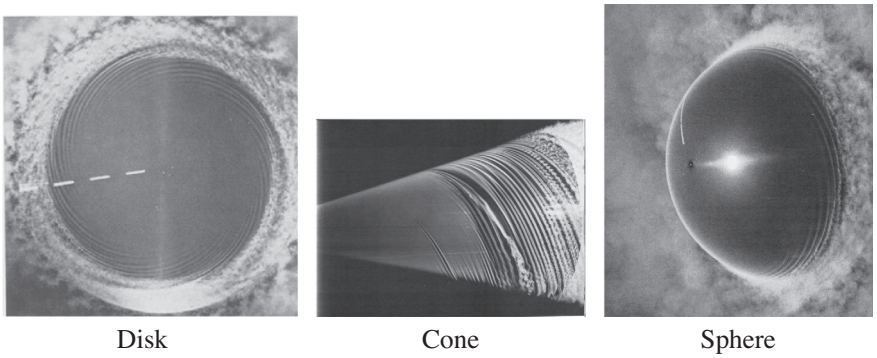

Fig. 1. Boundary-layer flow visualizations over a rotating disk, cone and sphere due to Kohoma, Kobayashi and co-workers Van Dyke (1982).

number with azimuthal wavenumber. Garrett & Peake concluded that the onset of the slow vortices was related to the switch in dominant mode to the type II mode and the appearance of the inflection point, although they were unable to determine a theoretical speed to compare to the observed $c = 0.76$. By artificially fixing $c = 0.76$ (using *method 2* as denoted in Garrett (2010a)), they were able to correctly predict properties of the slow vortices, i.e. critical Reynolds number, vortex number and angle of orientation. Garrett (2010c) revisited the problem of the vortex-speed selection and was able to predict a selection speed of $c = 0.75$ for a sphere rotating in otherwise still fluid. He also demonstrated that this speed increases slightly with incident axial flow. These predictions were obtained by extending the *method 2* approach to consider the linear amplification rates within the region of convective instability. The results demonstrated that, although the type II mode had larger amplification rates than the type I mode for large values of c, the globally maximum amplification rates within the convectively unstable region occurred for the type I mode with $c = 0.75$. This suggests that Garrett & Peake's earlier observation of slow vortices at the position of streamline-curvature dominance was merely coincidental. Garrett (2010a, 2010b, 2011) performed similar analyses of the boundary-layer flows over the family of rotating cones (including the disk at the limiting half-angle) and again found that type I modes travelling at 75% were the most amplified. Although naturally occurring surface roughness is known to prohibit the selection of travelling modes, Garrett's collection of work leads to the prediction that *slow vortices* traveling at a local speed of 75% would be selected over perfectly smooth disks, cones and spheres, where roughness would not act to select stationary modes.

Returning to the rotating-spheroid flow, we are unaware of any explicit studies of the stability and transition of rotating-spheroid boundary layers. However, Kohama (2000) briefly alludes to experiments on rotating concave-ogive-cones (which are related to spheroids) and notes that the concavity of the body surface acts to delay transition. Furthermore, we are unaware of any existing theoretical studies of the stability of rotating-spheroid flows. Our study therefore represents the first stability analyses in these rotating geometries and, unfortunately, we will not be able to compare our results to existing observations or calculations. However, we will see that our formulation is consistent with existing investigations into the rotating-sphere and -disk boundary layers and will demonstrate favorable comparisons with those studies in the limit of appropriate parameters. Although there is a substantial amount of literature available for the flow past a non-rotating prolate spheroid at various angle of attacks (see, for example, (Clarke, Brandner, & Walker, 2007; Tezuka & Suzuki, 2006)), these studies are not relevant to our current investigation. In particular, we are concerned entirely with the properties of the flow within the boundary layer over rotating spheroids, not the flow past a non-rotating body and the subsequent separation and wakes

This paper is structured as follows. In Section 2 we formulate the general rotating-spheroid problem, discussing briefly the governing partial differential equations (PDEs) for the steady flows (Samad & Garrett, 2010) and deriving the unsteady perturbation equations that govern their stability characteristics. We will see that a separate approach is required for the prolate and oblate geometries and the analysis of each geometry will be presented in turn. In Section 3, we present a detailed description of the analysis of the prolate geometry, considering both stationary and travelling convective modes. The equivalent study of the oblate geometry is presented in Section 4. Given the similarity of the two analyses, our presentation of the oblate case will be confined to a description of the results. The results are discussed in Section 5 and our conclusions are drawn in Section 6.

2. Governing equations

Our formulation and subsequent calculation of the steady boundary-layer flows over rotating prolate and oblate spheroids, parameterized by cross-sectional eccentricity e, has been published separately as Samad (2010) and Samad and Garrett (2010). However, we present a summary of the steady formulation in Section 2.1 for completeness before deriving the associated unsteady perturbation equations in the same geometries in Section 2.2.

2.1. Steady flows

The formulation for the prolate and oblate geometries are necessarily different, although related. In both cases a Cartesian frame of reference is used that is fixed in space and has origin located at the center of the body and the spheroid rotates with constant angular velocity $\Omega^\star$ about the z-axis (asterisks denote dimensional quantities). We introduce two distinct spheroidal coordinate systems $(\eta^\star, \theta, \phi)$ defined relative to the Cartesian coordinates as follows.

For the prolate geometry:

$$x^\star = \sqrt{\eta^{\star 2} - d_0^{\star 2}}\sin\theta\cos\phi, \quad y^\star = \sqrt{\eta^{\star 2} - d_0^{\star 2}}\sin\theta\sin\phi, \quad z^\star = \eta^\star\cos\theta.$$

For the oblate geometry:

$$x^\star = \eta^\star\sin\theta\cos\phi, \quad y^\star = \eta^\star\sin\theta\sin\phi, \quad z^\star = \sqrt{\eta^{\star 2} - d_0^{\star 2}}\cos\theta.$$

It is clear that $0 \leqslant \theta \leqslant 2\pi$ and $0 \leqslant \phi \leqslant 2\pi$ are required to sketch the complete body in both cases, although here we are concerned with hemi-spheriodal bodies. The quantity $\eta^\star$ is the distance of the normal at particular (θ, ϕ) to each body surface; the point of origin of $\eta^\star$ is not fixed because the two coordinate systems have no fixed origins. We notice that the semi-major axis of the cross-sectional ellipses are along the axis of rotation (the z-axis) in the prolate case and perpendicular to

the axis of rotation (z-axis) in the oblate case. Further, θ and ϕ are the angles which $\eta^\star$ make with the planes horizontal and vertical to the z-axis, respectively. The parameter $d^\star$ is the focal distance of each ellipse formed by the cross section of both types of spheroid. For a spheroid with constant cross-sectional eccentricity e, we must have $e = d^\star/\eta^\star \in [0.1)$. The geometries are summarized in Fig. 2. As shown, we consider particular spheroids, of constant semi-major axes of length $\eta_0^\star$, and, due to the symmetrical nature of each body, our analyses are carried out in the region $0 \leqslant \theta \leqslant \pi/2$ about each z-axis. Further, $d_0^\star$ is the corresponding constant focal distance of the cross-sectional ellipses of particular spheroids defined by $\eta_0^\star(\theta,\phi)$.

As detailed in Samad (2010), the Navier–Stokes and continuity equations are transformed to each spheroidal coordinate system using the transformations defined above. We then apply Prandtl's boundary-layer assumptions to obtain the dimensional boundary-layer equations that govern the laminar flow over the particular spheroid defined by the geometry (prolate or oblate) and e. In order to non-dimensionalize the equations we scale the velocities on the equatorial surface speed of the spheroid, as shown in Eq. (1). This is consistent with Garrett & Peake's original formulation of the rotating sphere.

$$U = \frac{U^\star}{\Omega^\star a^\star}, \quad V = \frac{V^\star}{\Omega^\star a^\star}, \quad W = \frac{W^\star}{(\nu^\star \Omega^\star)^{1/2}}. \tag{1}$$

Here $U(\eta,\theta;e)$, $V(\eta,\theta;e)$ and $W(\eta,\theta;e)$ are the scaled, steady, axisymmetric velocities in the θ-, ϕ- and η-directions respectively. Note that $a^\star$ is the equatorial radius of the body defined separately for each spheroid type:

$$a^\star = \begin{cases} \left(\eta_0^{\star 2} - d_0^{\star 2}\right)^{1/2} = \eta_0^\star\sqrt{1-e^2} & \text{prolate}, \\ \eta_0^\star & \text{oblate}. \end{cases} \tag{2}$$

Further, η is the distance through the boundary layer from the surface of the spheroid, scaled on the boundary-layer thickness $\delta^\star = (\nu^\star/\Omega^\star)^{1/2}$, such that $\eta = (\Omega^\star/\nu^\star)^{1/2}(\eta^\star - \eta_0^\star)$, where $\nu^\star$ is the coefficient of kinematic viscosity. Since we are considering spheroids that rotate within otherwise still fluid, the mean pressure $P^\star$ is constant and is neglected in this analysis.

In the prolate geometry, the resulting laminar-flow equations are

$$\begin{aligned} &W\frac{\partial U}{\partial \eta} + U\frac{\partial U}{\partial \theta} - V^2\cot\theta = \sqrt{\frac{1-e^2}{1-e^2\cos^2\theta}}\frac{\partial^2 U}{\partial \eta^2}, \\ &W\frac{\partial V}{\partial \eta} + U\frac{\partial V}{\partial \theta} + UV\cot\theta = \sqrt{\frac{1-e^2}{1-e^2\cos^2\theta}}\frac{\partial^2 V}{\partial \eta^2}, \\ &\frac{\partial W}{\partial \eta} + \frac{\partial U}{\partial \theta} + \left(\cot\theta + \frac{e^2\cos\theta\sin\theta}{1-e^2\cos^2\theta}\right)U = 0, \end{aligned} \tag{3}$$

and in the oblate geometry

$$\begin{aligned} &W\frac{\partial U}{\partial \eta} + \frac{1}{\sqrt{1-e^2}}\left(U\frac{\partial U}{\partial \theta} - V^2\cot\theta\right) = \sqrt{\frac{1-e^2}{1-e^2\sin^2\theta}}\frac{\partial^2 U}{\partial \eta^2}, \\ &W\frac{\partial V}{\partial \eta} + \frac{1}{\sqrt{1-e^2}}\left(U\frac{\partial V}{\partial \theta} + UV\cot\theta\right) = \sqrt{\frac{1-e^2}{1-e^2\sin^2\theta}}\frac{\partial^2 V}{\partial \eta^2}, \\ &\sqrt{1-e^2}\frac{\partial W}{\partial \eta} + \frac{\partial U}{\partial \theta} + \left(\cot\theta - \frac{e^2\cos\theta\sin\theta}{1-e^2\sin^2\theta}\right)U = 0. \end{aligned} \tag{4}$$

We note that in both geometries the limit $e \to 0$ reduces the laminar-flow equations to those for the rotating sphere, as found in the literature (see (Banks, 1965; Garrett & Peake, 2002), for example). The boundary conditions for both sets of Eqs. (3) and (4) are given by

$$\begin{aligned} &U = W = V - \sin\theta = 0 \quad \text{on } \eta = 0, \\ &U = V = 0 \quad \text{as } \eta \to \infty. \end{aligned} \tag{5}$$

These represent the non-slip boundary condition on the body surface and the quiescent fluid condition at the edge of the boundary layer, respectively.

As discussed in Samad (2010); Samad and Garrett (2010), the governing equations are solved using the NAG routine D03PEF to find the laminar flow at each latitude for a particular e in either geometry. This NAG routine is a general PDE solver that reduces the system of PDEs to a system of ODEs in η. The resulting system of ODEs is solved at each latitude by marching from a given complete solution at $\theta = 0^\circ$ towards the equator $\theta = 90^\circ$ in one degree increments. At each latitude a backward differentiation formula method is used over a regularly spaced grid of 2000 data points between $\eta = 0$ and $\eta = 20$. The initial solution at $\theta = 0^\circ$ is found using a series-solution method also described in Samad (2010) and Samad and Garrett (2010).

Fig. 3 shows the three velocity components for both geometries at latitudes of $\theta = 10^\circ$ and 70° as the eccentricity is varied. Note that at low latitudes the flow profiles are nearly indistinguishable for each e, but become more sensitive to e at higher latitudes. We find that the latitudinal velocity is inflectional at all latitudes and eccentricities which implies that the flows

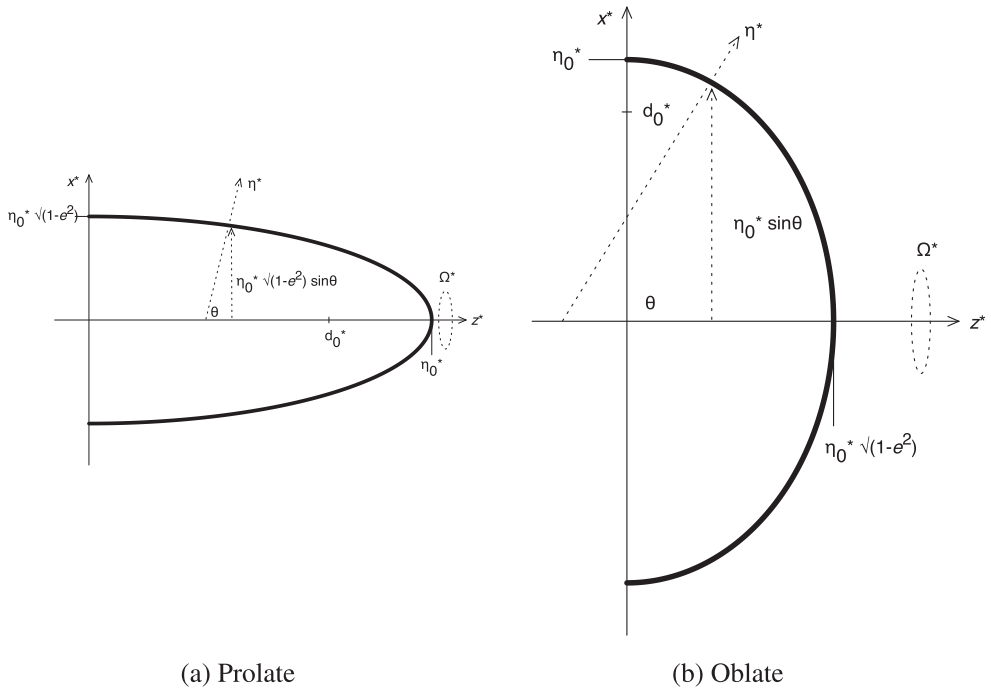

Fig. 2. Cross-sectional sketch of each spheroidal coordinate system.

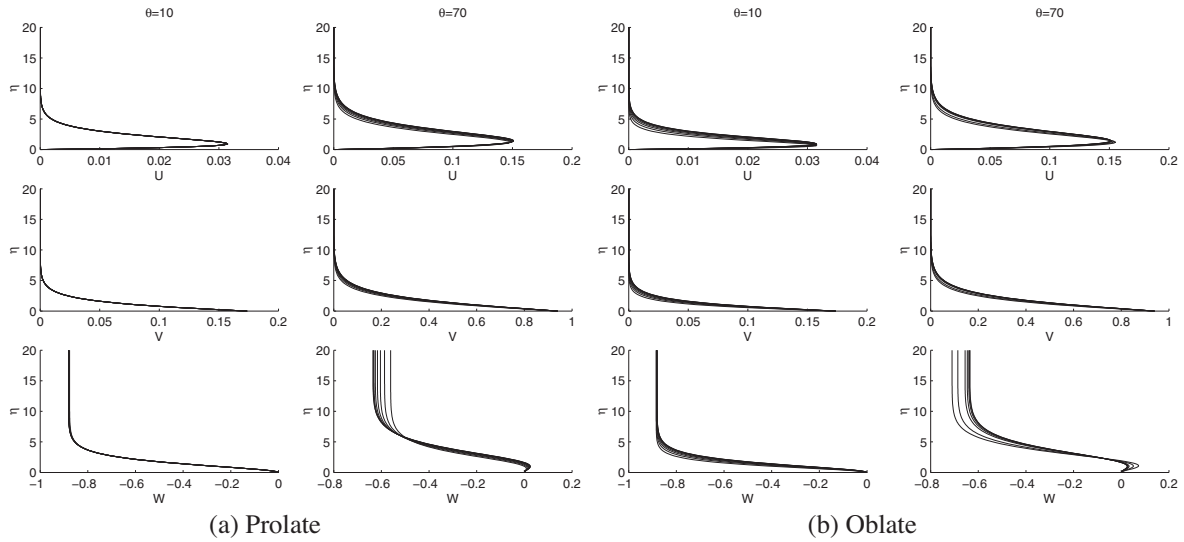

Fig. 3. Steady velocity profiles at latitudes $\theta = 10^\circ$ and 70° with increasing $e = 0$–0.7 in 0.1 increments (prolate: left to right in each frame; oblate: left to right for U and V, right to left for W). Taken from Samad and Garrett (2010).

are unstable to crossflow instabilities according to Rayleigh's theorem. We also note that fluid is entrained into the boundary layer at all latitudes through the negative W-component, but has a region of reverse flow close to the surface at latitudes beyond a critical value between $\theta = 60^\circ$–70°, depending on the geometry and value of e. The magnitude of the reverse flow is decreased with e at these high latitudes. The apparent lack of sensitivity to e is a consequence of the scalings used; recall that velocities are scaled on local the equatorial surface velocities $\Omega^\star a^\star$ and so in reality the unscaled velocity components would undergo significant stretching.

2.2. Perturbation equations

The stability analyses presented in Sections 3 & 4 will be conducted locally at points on the rotating spheroids. In each geometry the governing equations are formed by perturbing the steady flow (as found in Section 2.1) with the unsteady normal-mode quantities

$$(\hat{u}^\star,\ \hat{v}^\star,\ \hat{w}^\star,\ \hat{p}^\star)(\eta^\star,\ \theta,\ \phi;\ e) = (u^\star,\ v^\star,\ w^\star,\ p^\star)(\eta^\star; e)\exp\left(\mathrm{i}\left(\alpha^\star\int_0^\theta \mathrm{d}s^\star + \beta^\star r_\circ^\star\phi - \gamma^\star t^\star\right)\right). \tag{6}$$

Here $\mathrm{d}s^\star = \sqrt{\eta_0^{\star 2} - d^{\star 2} f(\theta)}\,\mathrm{d}\theta$ is an element of arc length in the latitudinal direction such that $\int_0^\theta \mathrm{d}s^\star$ is the arc length from the pole to the particular latitude under consideration with

$$f(\theta) = \begin{cases} \cos^2(\theta) & \text{prolate,} \\ \sin^2(\theta) & \text{oblate.} \end{cases} \tag{7}$$

$r_\circ^\star = a^\star \sin\theta$ is the local surface radius of the body at latitude θ.

The quantities $\alpha^\star$ and $\beta^\star$ are dimensional wavenumbers in the θ- and ϕ-directions respectively, and $\gamma^\star$ is the dimensional frequency. For a general spatio-temporal analysis $\alpha^\star = \alpha_r^\star + \mathrm{i}\alpha_i^\star$ and $\gamma^\star = \gamma_r^\star + \mathrm{i}\gamma_i^\star$ are complex quantities. In contrast, β is real to ensure periodicity around the azimuth of the spheroid at the particular latitude.

The perturbed-flow variables are substituted into the dimensional Navier–Stokes equations to form the dimensional perturbation equations. These are scaled on the typical length, velocity, time and pressure scales: $\delta^\star$, $a^\star\Omega^\star$, $\delta^\star/a^\star\Omega^\star$ and $\rho^\star(a^\star\Omega^\star)^2$ respectively, where $\rho^\star$ is the fluid density. The resulting non-dimensional equations are linearized by neglecting $O(R^{-2})$ terms, where

$$R = \frac{\delta^\star a^\star \Omega^\star}{\nu^\star} = \begin{cases} \frac{\delta^\star \eta_0^\star \Omega^\star}{\nu^\star}\sqrt{1-e^2} & \text{prolate,} \\ \frac{\delta^\star \eta_0^\star \Omega^\star}{\nu^\star} & \text{oblate.} \end{cases} \tag{8}$$

is the Reynolds number. Note that this Reynolds number is interpreted as a measure of the rotation rate of the particular spheroid under consideration, with the location of the analysis given by the particular θ. This is in contrast to equivalent studies of rotating disks and cones where the Reynolds number is interpreted as a measure of the radial location of the analysis for a particular rotation rate.

As R depends on e within the prolate analysis, care must be taken in any direct comparison between prolate spheroids of different eccentricities. With this in mind, we define the *spin Reynolds number*, Re, which eliminates the dependence on e and enables a direct comparison across bodies of comparable dimension (as defined by η_0) but different eccentricities, rotating at the same angular rate.

$$Re = \frac{\eta_0^{\star 2}\Omega^\star}{\nu^\star} = \begin{cases} \dfrac{R^2}{1-e^2} & \text{prolate,} \\ R^2 & \text{oblate.} \end{cases} \tag{9}$$

Furthermore, it is possible to define a *local Reynolds number* that is based on the local surface radius of the body. This is particularly useful for comparison with the rotating-disk and -cone studies (Garrett et al., 2009; Lingwood, 1995; Malik, 1986), for example. Again the effects of eccentricity are removed.

$$R_D = \begin{cases} \frac{R}{\sqrt{1-e^2}}\sin\theta & \text{prolate,} \\ R\sin\theta & \text{oblate.} \end{cases} \tag{10}$$

Following Garrett (2002), Garrett and Peake (2002, 2004, 2007), Garrett et al. (2009, 2010), Garrett (2010a, 2010b, 2010c) and Lingwood (1995) the perturbation equations for either geometry can be written as a set of six first-order ordinary differential equations using the transformed variables

$$\begin{aligned} \phi_1(\eta,\alpha,\beta,\gamma;\theta,R,e) &= \alpha_1 u + \beta v, \\ \phi_2(\eta,\alpha,\beta,\gamma;\theta,R,e) &= \alpha_1 u' + \beta v', \\ \phi_3(\eta,\alpha,\beta,\gamma;\theta,R,e) &= w, \\ \phi_4(\eta,\alpha,\beta,\gamma;\theta,R,e) &= p, \\ \phi_5(\eta,\alpha,\beta,\gamma;\theta,R,e) &= \alpha_1 v - \beta u, \\ \phi_6(\eta,\alpha,\beta,\gamma;\theta,R,e) &= \alpha_1 v' - \beta u'. \end{aligned}$$

The governing perturbation equations are stated in Appendix A, where α_1 is also defined for each geometry. Note that the subscripts v and s in perturbation equations indicate which of the $O(R^{-1})$ terms arise from viscous and streamline-curvature effects, respectively. Coriolis terms do not appear since a fixed frame of reference is used. By neglecting the $O(R^{-1})$ streamline-curvature terms we obtain the Orr–Sommerfeld Eq. (11) in each spheroid geometry. Further, neglecting both streamline-curvature and viscous terms leads to Rayleigh's Eq. (12). This study presents an analysis of the full system of

perturbation equations and the Rayleigh and Orr–Sommerfeld equations are shown here only to demonstrate the consistency of the full system with the standard equations of stability theory.

$$\frac{\mathrm{i}}{R}\left(M^3\phi_3'''' - 2M(\alpha^2+\beta^2)\phi_3'' + \frac{1}{M}(\alpha^2+\beta^2)^2\phi_3\right) + (\alpha U+\beta V-\gamma)\left(M\phi_3'' - \frac{(\alpha^2+\beta^2)}{M}\phi_3\right) - M(\alpha U''+\beta V'')\phi_3 = 0, \tag{11}$$

$$(\alpha U+\beta V-\gamma)\left(M\phi_3'' - \frac{1}{M}(\alpha^2+\beta^2)\phi_3\right) - M(\alpha U''+\beta V'')\phi_3 = 0, \tag{12}$$

where

$$M = \sqrt{\frac{1-e^2}{1-e^2 f(\theta)}} \tag{13}$$

with $f(\theta)$ defined by Eq. (7). Note that in the limit of $e \to 0$, all perturbation equations reduce to those derived by Garrett (2002), Garrett and Peake (2002, 2004) and Garrett (2010c) for the rotating sphere.

The derivations of the perturbation equations for the prolate and oblate geometries require that factors $1/(1+\sqrt{1-e^2}\eta/R)$ and $1/(1+\eta/R)$, respectively, are set to unity in an approximation similar to the parallel-flow approximation. This approximation limits the analysis to a local analysis at each θ and its validity is discussed in Section 5.

In the local stability analyses that follow, we suppose that the boundary-layer flow is not absolutely unstable at the particular θ so that we can reduce the imaginary part of the frequency γ to zero in the Briggs–Bers procedure (Briggs, 1964; Bers, 1975) and proceed with a spatial convective analysis. We then solve the eigenvalue problem defined by the relevant perturbation equations with the homogeneous boundary conditions

$$\phi_i = 0 \quad \text{on} \quad \eta = 0,$$
$$\phi_i \to 0 \quad \text{as} \quad \eta \to \infty,$$

where $i = 1, 2 \ldots 6$. Physically, these conditions are interpreted as the disturbance being confined within the boundary layer. The numerical techniques used here are an extension of those used by Lingwood and Garrett in their analyses of related geometries. In particular, for each particular spheroid, the system is solved for certain combinations of α, β and γ for each R at a particular latitude θ. From this we form the dispersion relation, $D(\alpha, \beta, \gamma; R, \theta, e) = 0$, at that location with the aim of studying the occurrence of convective instabilities. As the non-dimensional speed of the surface of the rotating spheroid is $\sin\theta$, vortices travelling at speed c relative to the spheroid surface can be modeled by equating $c\sin\theta$ with the disturbance phase velocity in the same (azimuthal) direction, γ_r/β, leading to $\gamma_r = c\beta\sin\theta$. This results in the dispersion relation $D(\alpha, \beta; c, R, \theta, e) = 0$. This approach has been denoted *method 2* by Garrett (2010a).

Solving the dispersion relation enables an investigation into the spatial branches within the convectively unstable region prior to their pinching and the occurrence of local absolute instability at some higher critical Reynolds number. In each case, spatial branches are calculated using a double-precision fixed-step-size, fourth-order Runge–Kutta integrator with Gram–Schmidt orthonormalization and a Newton–Raphson linear search procedure, using an amended version of the code originally developed by Lingwood. Details of the amended code can be found in Samad (2010), for example.

Experimental observations show that boundary-layer eruption close to the equator of the rotating sphere greatly disrupts the flow beyond $\theta = 80^\circ$; this can be seen in Fig. 1. Stability analyses will therefore be performed at latitudes $\theta = 10^\circ$ to 70° only.

3. Instability modes, rotating prolate spheroid

3.1. Stationary modes

Naturally occurring surface roughness is known to select stationary modes in the boundary-layer flows over related rotating geometries. We therefore begin by making the *a priori* assumption that spiral vortices rotate with the spheroid surface, which will be the case in most practical applications. Spatial branches for $c = 1$ have been calculated at $\theta = 10^\circ$–70° for $e = 0.0$–0.7.

As with the analyses of related geometries (Garrett & Peake, 2002, 2004, 2007; Garrett et al., 2009, 2010; Garrett, 2010a, 2010b, 2010c; Lingwood, 1995; Garrett, 2002), two spatial branches are found to determine the convective-instability characteristics at all latitudes and Reynolds numbers. These arise from crossflow (type I) and streamline-curvature (type II) effects. The detailed behavior of the branches is not discussed here, and the interested reader is referred to Garrett and Peake (2002) and Samad (2010) for a detailed description in the limiting case of $e = 0$ and for $e > 0$, respectively.

The angle that the phase fronts make with a circle parallel to the equator is denoted by ϵ, and is found from $\epsilon = \arctan(\beta/\alpha_r)$. The integer number of complete cycles of the disturbance round the azimuth is $n = \beta R\sin\theta$. We identify ϵ and n as being the angle and number of spiral vortices on the spheroid surface, respectively. Note that n and ϵ are experimentally observable quantities which motivates their use here. Neutral curves in the (Re, α_r)-, (Re, β)-, (Re, n)- and (Re, ϵ)-planes are shown in Figs. 4 and 5 at $\theta = 10^\circ$ and 60° for $0 \leqslant e \leqslant 0.7$. Furthermore, neutral curves at latitudes to

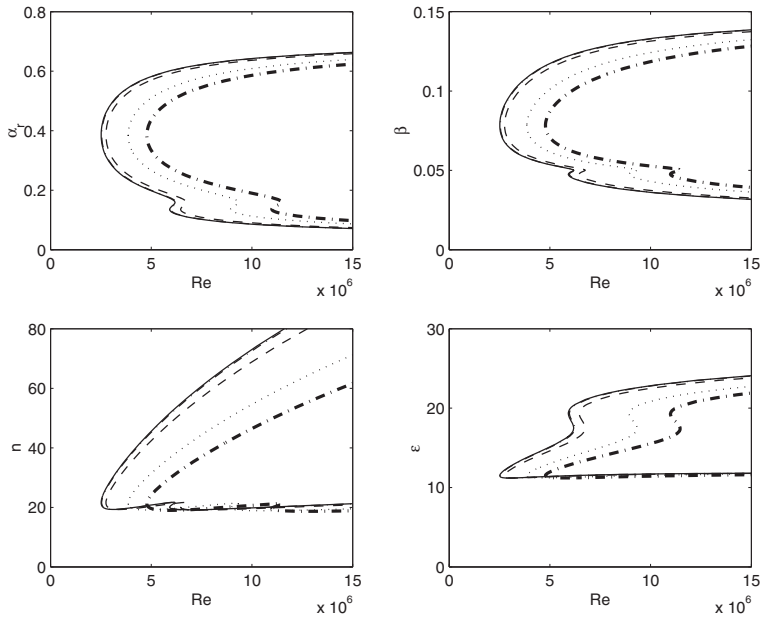

Fig. 4. Neutral curves in the (Re, α)-, (Re, β)-, (Re, n)- and (Re, ϵ)-planes at latitude 10° for $e = 0$ (–), 0.1 (-·-), 0.3(- -), 0.6 (···) & 0.7 (-·-).

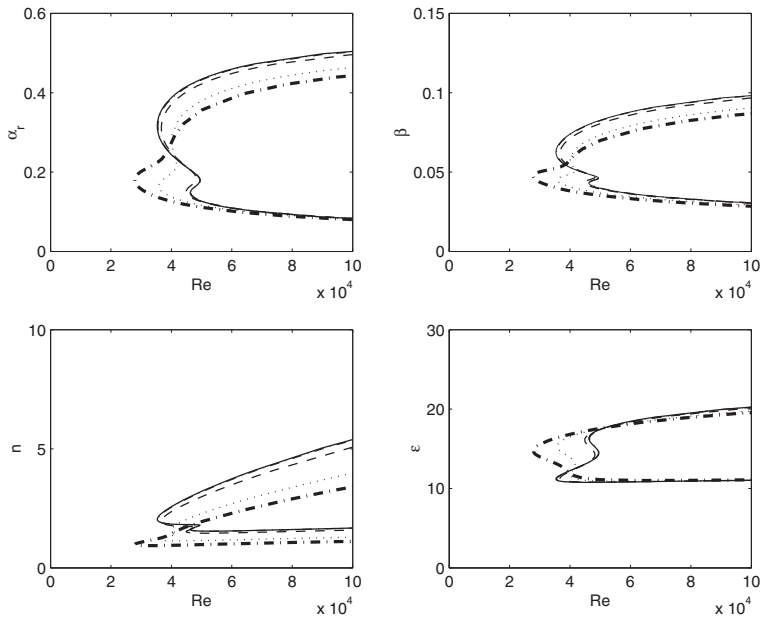

Fig. 5. Neutral curves for the prolate geometry in the (Re, α)-, (Re, β)-, (Re, n)- and (Re, ϵ)-planes at latitude 60° for $e = 0$ (–), 0.1 (-·-), 0.3(- -), 0.6 (···) & 0.7 (-·-).

$\theta = 70°$ (in increments of 10°) are given in Fig. 6 for $e = 0.0$, 0.3 and 0.7 in the (Re, α_r)-plane only. Note that the spin Reynolds number (9) has been used to facilitate a comparison across values of e within each geometry. Each neutral curve encloses a region that is convectively unstable, and we see the characteristic two-lobed structure for low to moderate latitudes which is also seen in the analysis of related geometries. The larger lobe, characterized by higher wavenumbers arises from the behavior of the type I branch; and the smaller lobe, characterized by smaller wavenumbers, from the type II branch.

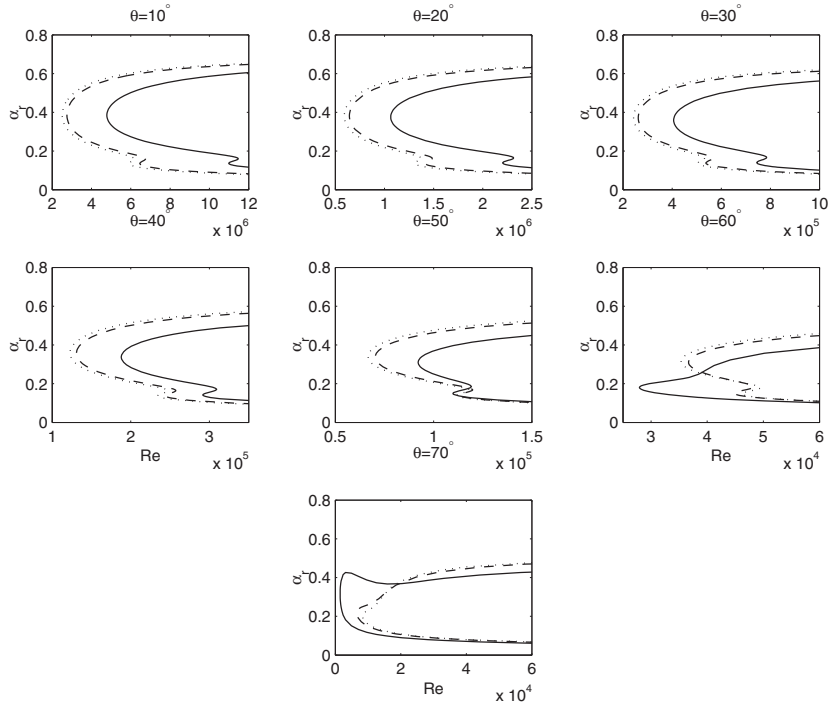

Fig. 6. Neutral curves for the prolate geometry in the (Re, α)-plane at all latitudes for $e = 0.0$ $(\cdots)$, 0.3 (--) & 0.7 (–).

Neutral curves shown in Figs. 4–6 are calculated using the full perturbation Eqs. (A.1)–(A.6). Neutral curves calculated using the Orr–Sommerfeld Eq. (11) were found to be single-lobed at each latitude for all values of e, with the critical Reynolds number lower than that for the most unstable mode arising from the full system. Although not shown here, neutral curves calculated from the full system and the Orr–Sommerfeld equation are found to be consistent for large Re for all parameter sets $\{\theta, e\}$.

Figs. 4–6 demonstrate that the effect of increased eccentricity on the relative importance of the type I mode is small at low θ. This reflects the insensitivity of the basic flows to e at low latitudes, see Fig. 3(a). We also see that the relative importance of the type II mode is increased for all e as the latitude is increased. For $\theta \leqslant 50^\circ$, the type I mode remains the most dangerous (in the sense of lowest critical Reynolds number) at each e considered; at $\theta = 60^\circ$, the type II becomes the most dangerous for sufficiently high e; and for $\theta = 70^\circ$, the type II lobe is seen to dominate at all eccentricities.

Fig. 6 demonstrates that increasing e increases the critical Reynolds numbers for the onset of both modes at latitudes $10^\circ \leqslant \theta < 50^\circ$, i.e. eccentricity acts as a stabilizing effect at low to moderate latitudes. However, at latitudes $\theta \geqslant 50^\circ$ the type II mode, which now has the lowest critical Reynolds number, is seen to become increasingly dangerous with increased e. Eccentricity is therefore seen to have a destabilizing effect at high latitudes with respect to critical Reynolds numbers. We do however note that increasing e acts to slightly narrow the region of convectively unstable parameters at all latitudes and so could be interpreted as a stabilizing effect in this sense. However, for high latitudes the reduced critical Reynolds number is expected to be the dominant characteristic. A comprehensive presentation of the critical Reynolds numbers for stationary disturbances is given in Table B.2.

We interpret these results as follows. Rotating prolate spheroids with high eccentricity first become convectively unstable at high latitudes for lower spin rates than are required for bodies with lower eccentricities, this is due to streamline-curvature effects. However, for the instability to manifest at lower latitudes, where crossflow effects dominate, a higher spin rate is required for bodies with larger eccentricity. Eccentricity is therefore interpreted as a destabilizing influence at high latitudes and stabilizing for moderate to low latitudes; this reflects the different response of the dominant instability mode at each latitude to changes in the local geometry of the body.

At all latitudes the neutral curves for $e = 0$ are as calculated by Garrett and Peake (2002) for the rotating sphere. When expressed in terms of the local Reynolds number (10), the neutral curves for small values of $e \leq 0.2$ limit to those for convective instability of the rotating-disk boundary layer (due to Malik (1986), for example) as θ tends towards the pole. This is of no surprise as, for low eccentricity, the region close to the pole is locally flat and so limits to a small rotating disk. For larger values of eccentricity, the behavior does not limit entirely to the rotating disk, reflecting the residual curvature in that region. The limiting behavior can be seen in Fig. 7 where it is clear that the effect of the residual curvature close to the pole is stabilizing for both mode types.

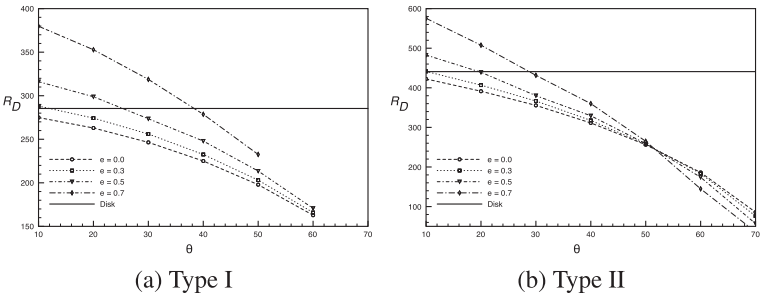

Fig. 7. A comparison of the critical R_D values for the onset of the type I and type II modes within the prolate geometry with those for the rotating disk (horizontal lines) Malik (1986).

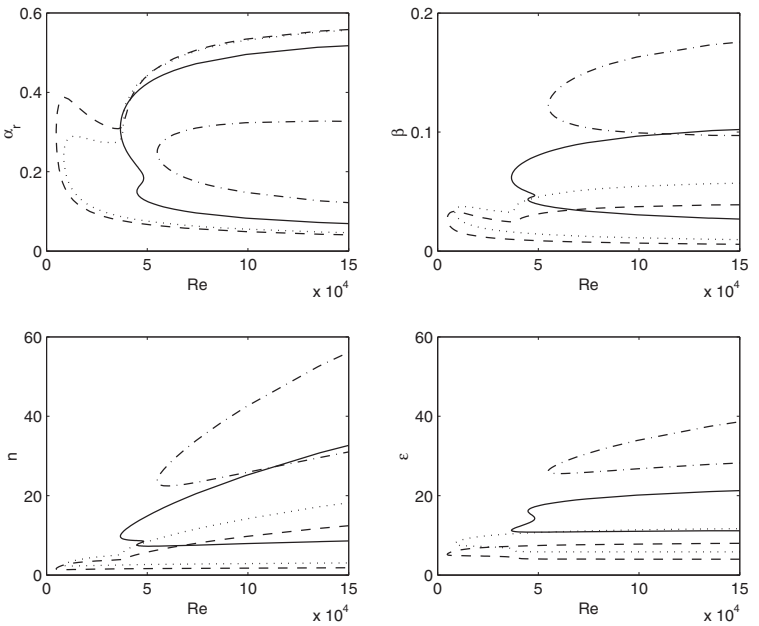

Fig. 8. Neutral curves for $\theta = 60^\circ$, $e = 0.3$ for travelling-mode disturbances with $c = 0.7$ (--), $c = 1$ (–), $c = 1.5$ (···), and $c = 2$ (--).

3.2. Travelling modes

Disturbance speeds have been considered in the range $c = 0.5$–9.0 relative to the body surface for each parameter set. Fig. 8 shows the resulting neutral curves at $\theta = 60^\circ$ for $e = 0.3$ in terms of α_r, β, n, and ϵ for $c = 0.7,\ 1,\ 1.5$ and 2. Recall that, for example, $c = 0.7$ corresponds to disturbances travelling at 70% of the local spheroid surface speed, and $c > 1$ correspond to disturbances travelling at speeds greater than the local surface of the spheroid. At this latitude and eccentricity, and indeed all those considered, we find that the lobe arising from the type II mode is sensitive to the disturbance speed. In particular, the type II lobe is quickly eliminated for $c < 1$ and exaggerated for $c > 1$.

The result that *quickly* travelling type II modes are the most dangerous (in the sense of lowest critical Reynolds number) is consistent with the previous theoretical results on the related geometries (Balakumar & Malik, 1991; Faller, 1991; Garrett, 2010a, 2010b, 2010c; Turkyilmazoglu & Gajjar, 1998). However, it is important to note that the range of waveangles and vortex numbers predicted to be unstable to quickly travelling modes is narrowed with increased c. In a sense this is a stabilizing effect because only a very narrow range of vortex parameters can be selected, and is much more significant than the slight narrowing mentioned in Section 3.1 in relation to stationary modes. We therefore have two competing factors in the vortex-speed selection process over all prolate spheroids: the critical Reynolds numbers for the onset of the type II mode reduce with increased c, but the range of parameter values that the corresponding vortices can exist at becomes increasingly narrow, thereby prohibiting selection. In order to clarify the process we follow Garrett (2010a, 2010b, 2010c) and consider the linear growth rates for traveling modes through the region of convective instability.

Although not shown in detail here, plots of the spatial branches at different values of c have been produced in order to visualize the growth rates, $-\alpha_i$, in all parameter combinations. The results show that the growth rates of the type II lobe

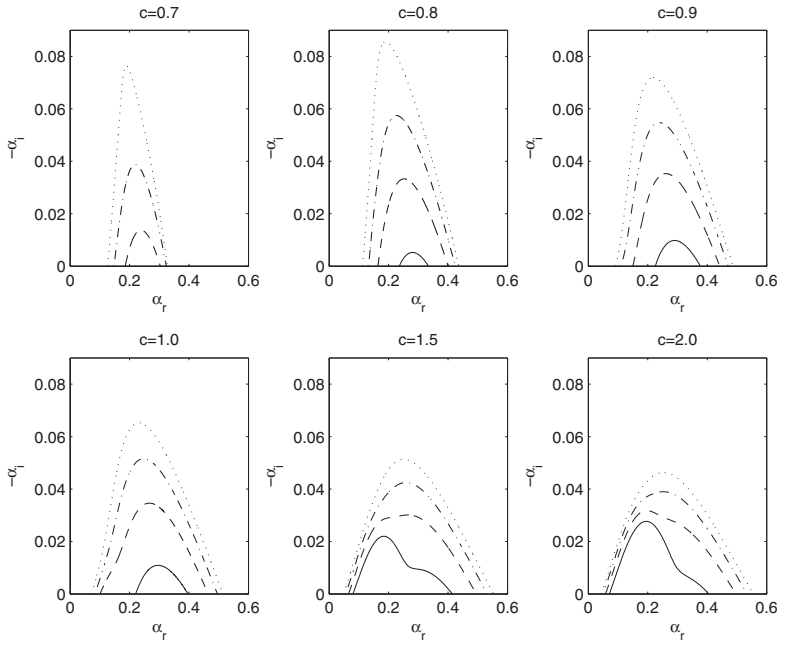

Fig. 9. Linear convective growth rates for the prolate geometry for travelling-mode disturbances with $c = 0.7$–2 for $\theta = 60^\circ$, $e = 0.3$ at $R = 200$ (–), $R = 250$ (--), $R = 300$ (-·-), $R = 352$ (···).

increase relative to the type I mode as c increases; however, more importantly, we note that the *globally maximum* growth rates for all parameter sets are for the type I mode. An example of this is shown in Fig. 9 in the particular case of $e = 0.3$ at $\theta = 60^\circ$. In each case we find that the growth rates are maximized for c between 0.7 and 0.8 at Reynolds numbers well within the convectively unstable regime. Further investigation reveals a clear peak in the maximum growth rate at $c = 0.75$ for all the parameter combinations tested. It is therefore likely that slow rotating vortices, moving at a speed of 75% of the local surface speed, will be selected over rotating prolate spheroids of all eccentricities where roughness elements are not present thereby enabling the existence of travelling modes in the convectively unstable region. It is interesting to note that this is entirely consistent with the results of Garrett (2010a, 2010b, 2010c, 2011) where similar analyses are presented for the related geometries and travelling type I modes with $c = 0.75$ are found to be the most amplified.

Despite the clear prediction that $c = 0.75$ well within the convectively unstable regime at each θ, we note, however, that for Reynolds numbers close to the critical values (where not all values of c are yet available for selection) the growth rates are maximize at higher values of c. For example, close inspection of the particular case shown in Fig. 9 shows the maximum growth to be at $c = 2$ at $R = 200$, and this tends to a value between $c = 0.7$ and $c = 0.8$ as R is increased. The prediction of high-speed modes is a consequence of the local analysis used and does not imply that high-speed modes would be selected in practice. In particular, since the unstable region moves to lower θ with increased R, the growth rate of a high-speed mode from an analysis at location θ_1 would, in practice, be dominated by the slow mode at nearby latitude $\theta_2 > \theta_1$.

Note that in producing plots of the spatial growth rates, such as that shown in Fig. 9, it is only possible to consider the convective instability at a particular latitude over a finite distance in R before a region of absolute instability is entered. Although we are able to consider the convective instability beyond this critical value by avoiding parameters within the region of absolute instability, eventually the position of maximum growth rate coincides with the location of a pinch point. At this point the characteristic branch exchange between the type I and type III branches occurs (Garrett & Peake, 2002; Lingwood, 1995) and the maximum spatial growth rate in the convective sense is undefined. Absolute instability is a spatio-temporal instability and so the region of absolute instability contained within the region of convective instability is irrespective of c. How far the convective instability analysis for maximum growth rates can be extended for each c, θ and e is determined by the occurrence of a pinch point in the absolutely unstable region with $\gamma = c\beta \sin\theta$.

4. Instability modes, rotating oblate spheroid

4.1. Stationary modes

Equivalent analyses to those presented in Section 3.1 have been performed across the family of rotating oblate spheroids. Our results show that again type I and type II modes of convective instability exist within the boundary-layer flows. However, in the oblate case, we find much lower sensitivity in our results to the eccentricity parameter e, this is despite a similar

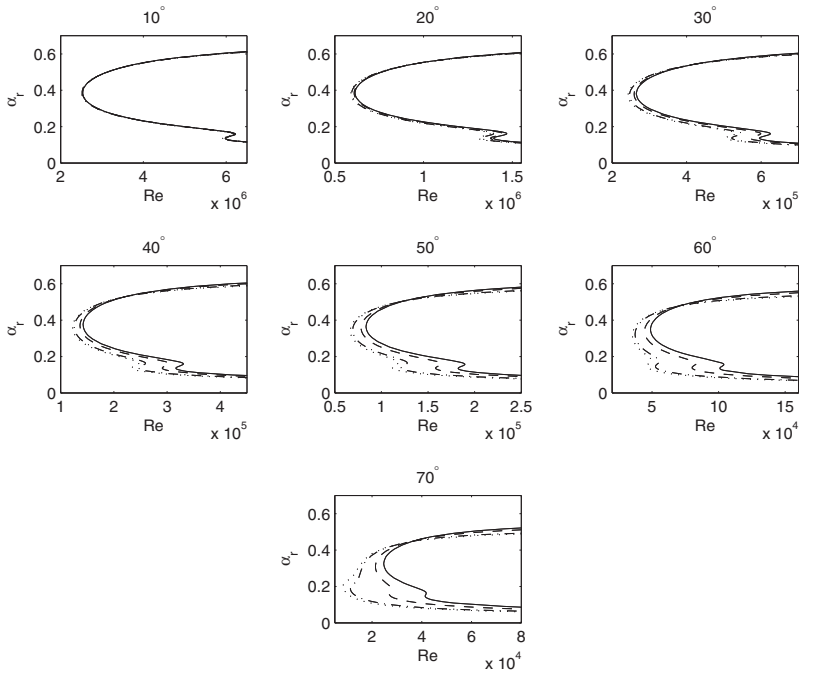

Fig. 10. Neutral curves of oblate in the (Re, α)-plane at all latitudes for $e = 0.0(\cdots)$, 0.3 (-·-), 0.6 (- -) & 0.7 (–).

sensitivity being observed for the steady-flow profiles in Fig. 3(b). Furthermore, the effect of increased e is found to be consistently stabilizing at all latitudes. This is again in contrast to the behavior found on the prolate body. Sample neutral curves are shown at all latitudes for various values of e in Fig. 10. The type I mode is consistently dominant for all parameter sets at latitudes below 70°, and the type II mode has a lower critical Reynolds number at $\theta = 70^\circ$ only for large e.

When expressed in terms of the local Reynolds number (10) we find that the boundary layer over the oblate spheroid is consistently more unstable than that over the rotating disk. Furthermore, the critical Reynolds numbers tend to the same limiting value for all values of e near to the pole, but this value is slightly lower than the corresponding values of the rotating disk. This can be seen in Fig. 11.

A comprehensive presentation of the critical Reynolds numbers for stationary disturbances is given in Table. We interpret these results as follows: rotating oblate spheroids with higher eccentricity become convectively unstable at all latitudes for higher spin rates than are required for lower eccentricities. Eccentricity is therefore interpreted as a stabilizing influence at all latitudes.

4.2. Travelling modes

Equivalent analyses to those presented in Section 3.2 have been performed across the family of rotating oblate spheroids in an attempt to predict the properties of the disturbances over smooth bodies. Our results in this geometry are similar to those in the prolate case. In particular, the shape of the neutral curve is dependent on the particular value of c considered,

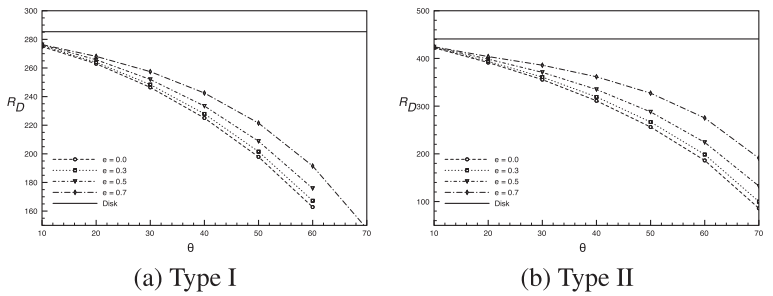

Fig. 11. A comparison of the critical R_D values for the onset of the type I and type II modes within the oblate geometry with those for the rotating disk (horizontal lines) Malik (1986).

with the type II lobe exaggerated for $c > 1$ and quickly eliminated for $c < 1$. The type II mode is therefore the most dangerous in the sense of critical Reynolds number for the quickly rotating disturbances. With respect to growth rates, again similar behavior is found to Section 3.2: despite the exaggerated parameter range and reduced critical Reynolds number for instability via the type II mode, the growth rates of the type I modes are still dominant. Again, the globally maximum growth rate for the dominant type I modes is seen to be at $c = 0.75$ for analyses at a sufficient distance into the region of convective instability.

5. Discussion

Instability modes of type I (crossflow) and II (streamline curvature) have been found to exist at all latitudes for spheroids of all eccentricities from both families. The results of both analyses have shown qualitatively similar behavior to that found on rotating disks (Lingwood, 1995; Malik, 1986) and spheres (Barrow & Garrett, 2013; Garrett & Peake, 2002), and quantitative agreement in appropriate limits. An important difference between the two types of spheroid, however, is the response of the type II mode to eccentricity. For oblate spheroids, eccentricity is seen to be stabilizing to both modes at all latitudes. For prolate spheroids, increased eccentricity is seen to be stabilizing to both modes at low latitudes ($\theta < 50^\circ$), but destabilizing to the type II mode at high latitudes ($\theta > 50^\circ$). In an attempt to explain this, one must consider the local curvatures of the two geometries relative to that of the sphere. Recall that for the sphere, $e = 0$ and the local curvature is constant at all θ; in this case we find the type II lobe to be dominant for latitudes above 70°. However, when $e \neq 0$ the resulting spheroids have a local curvature that depends on latitude

$$\kappa(\theta; e) = \begin{cases} \dfrac{\sqrt{1-e^2}}{\left(1-e^2\cos^2\theta\right)^{3/2}} & \text{prolate}, \\ \dfrac{\sqrt{1-e^2}}{\left(1-e^2\sin^2\theta\right)^{3/2}} & \text{oblate}, \end{cases} \tag{14}$$

In the prolate case, the local curvature is greater that of the sphere at all latitudes below $\theta = 50^\circ$, as seen in Fig. 12(a). Above this latitude the local curvature is seen to be less than that of the sphere, and we suggest that it is this effect that destabilizes the type II mode with increased e. The effect of local curvature is different in the oblate case (Fig. 12(b)) and such "negative" curvature relative to the sphere occurs only at latitudes below $\theta = 40$ where the type II is known to be only weakly amplified.

In the derivation of the governing perturbation equations, factors

$$\begin{cases} 1/\left(1+\sqrt{1-e^2}\eta/R\right) & \text{prolate}, \\ 1/(1+\eta/R) & \text{oblate}. \end{cases}$$

have been replaced by unity. This approximation is similar to the parallel-flow approximation found in many other boundary-layer investigations and, after conducting the stability analyses, we are able to comment on the validity of the approximation for various combinations of parameters. As shown in Fig. 3, at low latitudes the boundary layer is seen to be fully developed at around $\eta = 5$, but at higher latitudes it is seen to be fully developed only above $\eta = 10$; this is true for both geometries. This thickening of the boundary layer, together with the fact that the critical Reynolds numbers decrease with increased latitude, means that our approximation is less valid near to the equator and for large e. The inaccuracy is smallest near to the pole for oblate spheroids of low eccentricity where, at $\theta = 10^\circ$ for $e = 0.0$, for example, the onset of convective instability occurs at $R \approx 1600$. In this case, the factor is approximated by unity with an inaccuracy of about 0.3%. At $\theta = 70^\circ$ the convective instability in the analysis of the prolate spheroid with high eccentricity has a critical Reynolds number of $R \approx 30$. Here we see that the factor is approximated by unity with an error of around 20%. Although the inaccuracy caused by this approximation grows substantially as the analysis moves towards the equator for large eccentricities, it is the author's opinion that it will not affect the qualitative conclusions of this work.

It is acknowledged that this work consists of a linear analysis and so the predictions would be inaccurate in situations where the growth rates are large and non-linear effects would occur. However, we have predicted the properties of vortices

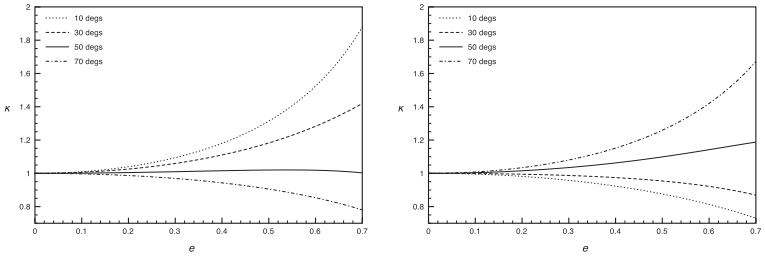

(a) Prolate (b) Oblate

Fig. 12. Local curvature (Eq. (14)) as a function of eccentricity.

from the very onset of convective instability where growth rates are small. Non-linearity would affect the breakdown of the vortices deep within the convectively unstable regime, but not their initial selection.

A number of open issues remain. For instance, experiments will be required in order to investigate the validity of the predictions made here for general e within both geometries. It is also clear that additional effects need to be included in our analysis, such as the presence of compressibility and enforced axial flow, before the results can be considered as representative models of the motivating industrial flows discussed in Section 1. Furthermore, in considering the growth rates through the convectively unstable region, we have found pinch points indicative of local absolute instability for sufficiently large Reynolds numbers (or rotation rates); this warrants further investigation with regards its possible role in transition to turbulence. Work is under way in each of these directions.

6. Conclusion

We have conducted local convective instability analyses of the boundary-layer flow over rotating prolate and oblate spheroids, with particular bodies defined by an eccentricity parameter e. This paper should be viewed as a generalization of Garrett and co-worker's previous work (Barrow & Garrett, 2013; Garrett & Peake, 2002; Garrett, 2010a) where $e = 0$. Our results in both geometries reproduce those for the rotating sphere when $e \to 0$ and we also find consistency with existing results for the rotating-disk flow as $\theta \to 0$.

Our results suggest that eccentricity has a universally stabilizing effect at all latitudes below approximately 50° on both spheroidal families. Above this latitude, effects of local curvature lead to different behavior for the prolate and oblate spheroids. In the case of a prolate body, eccentricity acts to destabilize flow; in the case of an oblate body, eccentricity continues to be a stabilizing effect.

The physical interpretation of the results are as follows. For a prolate body, we would expect that lower rotation rates are required for the flow to first become convectively unstable at higher latitudes for bodies with larger e, however higher rotation rates would then be required to move the transition region closer to the pole for bodies with larger e. For the oblate case, lower rotation rates are required at all latitudes for bodies with lower eccentricity. In both cases, the convective instability would manifest as co-rotating vortices, characteristic of the crossflow instability.

We are unaware of any experimental investigations into the rotating-spheroid flows considered here and are therefore currently unable to compare our results with experiments. We do however note Kohama's (Kohama, 2000) comment that concavity acts to delay the transition of the boundary-layer flow over concave-ogive-cones; our results are qualitatively consistent with his comment. A detailed set of predicted critical Reynolds numbers is presented in B to enable comparison with future experimental studies.

We have also shown that *slow* vortices are the most amplified and are likely to be selected in experiments where perfectly smooth spheroids are used. Although this is unlikely to be the case in most practical applications where surface roughness would be unavoidable and stationary vortices selected, the discovery is consistent with the unusual observation by Kobayashi and Arai (1990) of vortices travelling at 76% of the sphere surface in particular conditions. It is interesting to note that the same vortex-speed selection process has been demonstrated in the boundary-layer flow over rotating disks and cones (Garrett, 2010a, 2010b, 2010c; Garrett, 2011). Although experiments on smooth rotating disks have been reported by Corke and co-workers Corke and Knasiak (1998) and Othman and Corke (2006) where non-stationary modes have been observed, their results cannot be interpreted in terms of a particular vortex speed. Further experiments similar to Kobayashi and Arai (1990) are therefore required for all geometries to test these theoretical predictions.

AS would like to thank the University of Peshawar, Pakistan for financial support during this ongoing project.

Appendix A. Perturbation equations

A.1. Prolate geometry

$$\phi_1' = \phi_2 \tag{A.1}$$

$$\begin{aligned}\left[\frac{M^2\phi_2'}{R}\right]_v &= \frac{1}{R}\left(\left[\alpha^2+\beta^2\right]_v + \mathrm{i}R(\alpha U+\beta V-\gamma)\right)\phi_1 + \left[\frac{MW\phi_2}{R}\right]_s + \left(M(\alpha_1 U'+\beta_1 V') + \left[\frac{M^2\alpha_1 U+\beta V}{R\sqrt{1-e^2\cos^2\theta}}\right]_s\right)\phi_3 \\ &\quad + \mathrm{i}\left(\alpha^2+\beta^2 - \left[\frac{\mathrm{i}M\alpha}{R}\left(\frac{e^2\sin\theta\cos\theta}{1-e^2\cos^2\theta}+\cot\theta\right)\right]_s\right)\phi_4 - \left[\frac{M\cot\theta V\phi_5}{R}\right]_s \\ &\quad + \frac{M}{R}\left[\left(\alpha_1\frac{\partial U}{\partial\theta}+\beta\frac{\partial V}{\partial\theta}\right)u - (\alpha_1 V-\beta U)\cot\theta v\right]_s\end{aligned} \tag{A.2}$$

$$M\phi_3' = -\mathrm{i}\phi_1 - \left[\frac{2-e^2(1+\cos^2\theta)}{R(1-e^2\cos^2\theta)^{3/2}}\phi_3\right]_s \tag{A.3}$$

$$M\phi_4' = \left[\frac{\mathrm{i}W\phi_1}{R}\right]_s - \left[\frac{\mathrm{i}M\phi_2}{R}\right]_v + \left[\frac{2\left(M^2Uu+Vv\right)}{R\sqrt{1-e^2\cos^2\theta}}\right]_s - \frac{1}{R}\left(\left[\alpha^2+\beta^2\right]_v + \mathrm{i}R(\alpha U+\beta V-\gamma) + \left[M\left(W'+\frac{e^2\cos\theta\sin\theta}{(1-e^2\cos^2\theta)}U\right)\right]_s\right)\phi_3 \tag{A.4}$$

$$\phi_5' = \phi_6 \tag{A.5}$$

$$\left[\frac{M^2\phi_6'}{R}\right]_v = \left[\frac{V\cot\theta\phi_1}{R}\right]_s + \left(M(\alpha_1V'-\beta U') + \left[\frac{1}{R}\left(\frac{\alpha_1V}{\sqrt{1-e^2\cos^2\theta}} - \frac{M\beta U}{(1-e^2\cos^2\theta)}\right)\right]_s\right)\phi_3 + \left[\frac{\beta M}{R}\left(\frac{e^2\cos\theta\sin\theta}{1-e^2\cos^2\theta}+\cot\theta\right)\phi_4\right]_s + \frac{1}{R}\left(\left[\alpha^2+\beta^2\right]_v + \mathrm{i}R(\alpha U+\beta V-\gamma)\right)\phi_5 + \left[\frac{MW\phi_6}{R}\right]_s + \left[\frac{M}{R}\left(\left(\alpha_1\frac{\partial V}{\partial\theta}-\beta\frac{\partial U}{\partial\theta}\right)u + \cot\theta(\alpha_1U+\beta V)v\right)\right]_s. \tag{A.6}$$

Where a prime denotes differentiation with respect to η and

$$\alpha_1 = \alpha - \left[\frac{\mathrm{i}M}{R}\right]_s\left(\frac{e^2\sin\theta\cos\theta}{1-e^2\cos^2\theta}+\cot\theta\right).$$

The quantity M is defined by Eq. (13).

Note that the perturbation velocities u and v are expressed in terms of ϕ_1 and ϕ_2 via

$$u = \frac{1}{\alpha_1^2+\beta^2}(\alpha_1\phi_1-\beta\phi_5), \quad v = \frac{1}{\alpha_1^2+\beta^2}(\alpha_1\phi_5+\beta\phi_1).$$

A.2. Oblate geometry

$$\phi_1' = \phi_2 \tag{A.7}$$

$$\left[\frac{M^2\phi_2'}{R}\right]_v = \frac{1}{R}\left(\left[\alpha^2+\beta^2\right]_v + \mathrm{i}R(\alpha U+\beta V-\gamma)\right)\phi_1 + \left[\frac{MW\phi_2}{R}\right]_s + \left(M(\alpha_1U'+\beta_1V') + \left[\frac{1}{R}\left(M\alpha_1U+\frac{\beta V}{\sqrt{1-e^2\sin^2\theta}}\right)\right]_s\right)\phi_3 + \mathrm{i}\left(\alpha^2+\beta^2 - \left[\frac{\mathrm{i}\alpha}{R}\left(\frac{-e^2\sin\theta\cos\theta}{(1-e^2\sin^2\theta)^{3/2}}+\frac{\cot\theta}{\sqrt{1-e^2\sin^2\theta}}\right)\right]_s\right)\phi_4 - \left[\frac{\cot\theta V\phi_5}{R\sqrt{1-e^2\sin^2\theta}}\right]_s + \frac{1}{R\sqrt{1-e^2\sin^2\theta}}\left[\left(\alpha_1\frac{\partial U}{\partial\theta}+\beta\frac{\partial V}{\partial\theta}\right)u - (\alpha_1V-\beta U)\cot\theta\, v\right]_s \tag{A.8}$$

$$M\phi_3' = -\mathrm{i}\phi_1 - \left[\frac{M(2-e^2\sin^2\theta)}{R(1-e^2\sin^2\theta)}\phi_3\right]_s \tag{A.9}$$

$$M\phi_4' = \left[\frac{\mathrm{i}W\phi_1}{R}\right]_s - \left[\frac{\mathrm{i}M\phi_2}{R}\right]_v + \left[\frac{2M}{R}\left(\frac{Uu}{(1-e^2\sin^2\theta)}+Vv\right)\right]_s - \frac{1}{R}\left(\left[\alpha^2+\beta^2\right]_v + \mathrm{i}R(\alpha U+\beta V-\gamma) + \left[MW' - \frac{e^2\sin\theta\cos\theta}{(1-e^2\sin^2\theta)^{3/2}}U\right]_s\right)\phi_3 \tag{A.10}$$

$$\phi_5' = \phi_6 \tag{A.11}$$

$$\left[\frac{M^2\phi_6'}{R}\right]_v = \left[\frac{V\cot\theta\phi_1}{R\sqrt{1-e^2\sin^2\theta}}\right]_s + \left(M(\alpha_1 V' - \beta U') + \left[\frac{1}{R}\left(\frac{\alpha_1 V}{\sqrt{1-e^2\sin^2\theta}} - \frac{M\beta U}{(1-e^2\sin^2\theta)}\right)\right]_s\right)\phi_3$$
$$+ \left[\frac{\beta}{R}\left(\frac{-e^2\cos\theta\sin\theta}{(1-e^2\sin^2\theta)^{3/2}} + \frac{\cot\theta}{\sqrt{1-e^2\sin^2\theta}}\right)\phi_4\right]_s + \frac{1}{R}\left(\left[\alpha^2+\beta^2\right]_v + \mathrm{i}R(\alpha U + \beta V - \gamma)\right)\phi_5 + \left[\frac{MW\phi_6}{R}\right]_s$$
$$+ \left[\frac{1}{R\sqrt{1-e^2\sin^2\theta}}\left(\left(\alpha_1\frac{\partial V}{\partial\theta} - \beta\frac{\partial U}{\partial\theta}\right)u + \cot\theta(\alpha_1 U + \beta V)v\right)\right]_s \tag{A.12}$$

Here

$$\alpha_1 = \alpha - \left[\frac{\mathrm{i}M}{R}\right]_s\left(\frac{-e^2\sin\theta\cos\theta}{(1-e^2\sin^2\theta)^{3/2}} + \frac{\cot\theta}{\sqrt{1-e^2\sin^2\theta}}\right)$$

and the quantity M is defined in Eq. (13).

Appendix B. Critical Reynolds numbers for stationary disturbances

The below tables give the critical spin Reynolds numbers, *Re*, for the onset of stationary modes of instability at eccentricity *e*. The subscripts I and II indicate that the critical value is for the onset of the type I and type II modes, respectively, and the most dangerous mode is indicated in bold. A "–" indicates that the crossflow lobe is not seen at the particular parameter values.

Tables B.1, B.2

Table B.1
Critical spin Reynolds numbers for the onset of convective instability modes within the prolate geometry. The bold text indicates the instability mode with lowest critical Reynolds number.

e	θ	Re_{I}	Re_{II}	e	θ	Re_{I}	Re_{II}
0.0	10	$\mathbf{2.51\times10^6}$	5.92×10^6		10	$\mathbf{2.97\times10^6}$	6.96×10^6
	20	$\mathbf{5.91\times10^5}$	1.31×10^6		20	$\mathbf{6.91\times10^5}$	1.51×10^6
	30	$\mathbf{2.43\times10^5}$	5.06×10^5		30	$\mathbf{2.79\times10^5}$	5.66×10^5
	40	$\mathbf{1.23\times10^5}$	2.34×10^5	0.4	40	$\mathbf{1.38\times10^5}$	2.52×10^5
	50	$\mathbf{6.67\times10^4}$	1.12×10^5		50	$\mathbf{7.34\times10^4}$	1.14×10^5
	60	$\mathbf{3.53\times10^4}$	4.62×10^4		60	$\mathbf{3.77\times10^4}$	4.32×10^4
	70	–	$\mathbf{8.35\times10^3}$		70	–	$\mathbf{5.20\times10^3}$
0.1	10	$\mathbf{2.54\times10^6}$	5.97×10^6		10	$\mathbf{3.31\times10^6}$	7.73×10^6
	20	$\mathbf{5.96\times10^5}$	1.32×10^6		20	$\mathbf{7.63\times10^5}$	1.65×10^6
	30	$\mathbf{2.45\times10^5}$	5.09×10^5		30	$\mathbf{2.99\times10^5}$	5.78×10^5
	40	$\mathbf{1.23\times10^5}$	2.35×10^5	0.5	40	$\mathbf{1.49\times10^5}$	2.62×10^5
	50	$\mathbf{6.70\times10^4}$	1.12×10^5		50	$\mathbf{7.77\times10^4}$	1.14×10^5
	60	$\mathbf{3.55\times10^4}$	4.65×10^4		60	$\mathbf{3.89\times10^4}$	4.04×10^4
	70	–	$\mathbf{8.16\times10^3}$		70	–	$\mathbf{3.68\times10^3}$
0.2	10	$\mathbf{2.61\times10^6}$	6.15×10^6		10	$\mathbf{3.86\times10^6}$	8.94×10^6
	20	$\mathbf{6.13\times10^5}$	1.35×10^6		20	$\mathbf{8.77\times10^5}$	1.86×10^6
	30	$\mathbf{2.51\times10^5}$	5.20×10^5		30	$\mathbf{3.44\times10^5}$	6.63×10^5
	40	$\mathbf{1.26\times10^5}$	2.39×10^5	0.6	40	$\mathbf{1.64\times10^5}$	2.76×10^5
	50	$\mathbf{6.83\times10^4}$	1.13×10^5		50	$\mathbf{8.38\times10^4}$	1.14×10^5
	60	$\mathbf{3.60\times10^4}$	4.59×10^4		60	4.01×10^4	$\mathbf{3.61\times10^4}$
	70	–	$\mathbf{7.56\times10^3}$		70	–	$\mathbf{2.34\times10^3}$
0.3	10	$\mathbf{2.75\times10^6}$	6.46×10^6		10	$\mathbf{4.78\times10^6}$	1.10×10^7
	20	$\mathbf{6.43\times10^5}$	1.41×10^6		20	$\mathbf{1.06\times10^6}$	2.20×10^6
	30	$\mathbf{2.62\times10^5}$	5.38×10^5		30	$\mathbf{4.06\times10^5}$	7.45×10^5
	40	$\mathbf{1.31\times10^5}$	2.44×10^5	0.7	40	$\mathbf{1.88\times10^5}$	3.14×10^5
	50	$\mathbf{7.03\times10^4}$	1.13×10^5		50	$\mathbf{9.21\times10^4}$	1.20×10^5
	60	$\mathbf{3.67\times10^4}$	4.49×10^4		60	-	$\mathbf{2.79\times10^4}$
	70	–	$\mathbf{6.56\times10^3}$		70	–	$\mathbf{1.47\times10^3}$

Table B.2
Critical spin Reynolds numbers for the onset of convective instability modes within the oblate geometry. The bold text indicates the instability mode with lowest critical Reynolds number.

e	θ	Re_{I}	Re_{II}	e	θ	Re_{I}	Re_{II}
0.0	10	$\mathbf{2.51 \times 10^6}$	5.92×10^6		10	$\mathbf{2.52 \times 10^6}$	5.95×10^6
	20	$\mathbf{5.91 \times 10^5}$	1.31×10^6		20	$\mathbf{6.00 \times 10^5}$	1.34×10^6
	30	$\mathbf{2.43 \times 10^5}$	5.06×10^5		30	$\mathbf{2.50 \times 10^5}$	5.34×10^5
	40	$\mathbf{1.23 \times 10^5}$	2.34×10^5	0.4	40	$\mathbf{1.28 \times 10^5}$	2.57×10^5
	50	$\mathbf{6.67 \times 10^4}$	1.12×10^5		50	$\mathbf{7.14 \times 10^4}$	1.29×10^5
	60	$\mathbf{3.53 \times 10^4}$	4.62×10^4		60	$\mathbf{3.89 \times 10^4}$	5.83×10^4
	70	–	$\mathbf{8.35 \times 10^3}$		70	–	$\mathbf{1.42 \times 10^4}$
0.1	10	$\mathbf{2.51 \times 10^6}$	5.92×10^6		10	$\mathbf{2.53 \times 10^6}$	5.97×10^6
	20	$\mathbf{5.91 \times 10^5}$	1.31×10^6		20	$\mathbf{6.04 \times 10^5}$	1.36×10^6
	30	$\mathbf{2.43 \times 10^5}$	5.08×10^5		30	$\mathbf{2.54 \times 10^5}$	5.50×10^5
	40	$\mathbf{1.23 \times 10^5}$	2.36×10^5	0.5	40	$\mathbf{1.32 \times 10^5}$	2.72×10^5
	50	$\mathbf{6.70 \times 10^4}$	1.13×10^5		50	$\mathbf{7.43 \times 10^4}$	1.41×10^5
	60	$\mathbf{3.56 \times 10^4}$	4.69×10^4		60	$\mathbf{4.12 \times 10^4}$	6.69×10^4
	70	–	$\mathbf{8.64 \times 10^3}$		70	–	$\mathbf{1.90 \times 10^4}$
0.2	10	$\mathbf{2.52 \times 10^6}$	5.93×10^6		10	$\mathbf{2.53 \times 10^6}$	5.98×10^6
	20	$\mathbf{5.93 \times 10^5}$	1.32×10^6		20	$\mathbf{6.09 \times 10^5}$	1.86×10^6
	30	$\mathbf{2.45 \times 10^5}$	5.13×10^5		30	$\mathbf{2.59 \times 10^5}$	5.71×10^5
	40	$\mathbf{1.24 \times 10^5}$	2.10×10^5	0.6	40	$\mathbf{1.64 \times 10^5}$	2.91×10^5
	50	$\mathbf{6.77 \times 10^4}$	1.16×10^5		50	$\mathbf{7.83 \times 10^4}$	1.58×10^5
	60	$\mathbf{3.62 \times 10^4}$	4.89×10^4		60	$\mathbf{4.44 \times 10^4}$	8.02×10^4
	70	–	$\mathbf{9.56 \times 10^3}$		70	$\mathbf{2.14 \times 10^4}$	2.70×10^4
0.3	10	$\mathbf{2.52 \times 10^6}$	5.94×10^6		10	$\mathbf{2.53 \times 10^6}$	5.98×10^6
	20	$\mathbf{5.96 \times 10^5}$	1.33×10^6		20	$\mathbf{6.14 \times 10^6}$	1.39×10^6
	30	$\mathbf{2.47 \times 10^5}$	5.21×10^5		30	$\mathbf{2.65 \times 10^5}$	5.95×10^5
	40	$\mathbf{1.26 \times 10^5}$	2.47×10^5	0.7	40	$\mathbf{1.42 \times 10^5}$	3.16×10^5
	50	$\mathbf{6.92 \times 10^4}$	1.21×10^5		50	$\mathbf{8.36 \times 10^4}$	1.83×10^5
	60	$\mathbf{3.73 \times 10^4}$	5.26×10^4		60	$\mathbf{4.89 \times 10^4}$	1.01×10^5
	70	–	$\mathbf{1.13 \times 10^4}$		70	$\mathbf{2.47 \times 10^4}$	4.14×10^4

References

Balakumar, P., & Malik M. R. (1991). Waves produced from a harmonic point source in a supersonic boundary layer. AIAA Pap. No. 91.

Banks, W. H. H. (1965). The boundary layer on a rotating sphere. *Quarterly Journal of Mechanics and Applied Mathematics, 48*, 443–454.

Banks, W. H. H. (1976). The laminar boundary layer on a rotating sphere. *Acta Mechanica, 24*, 273–287.

Barrow, A., & Garrett, S. J. (2013). The stability and transition of the boundary-layer flow over rotating spheres with surface mass flux and incident axial flow. *European Journal of Mechanics B, 38*, 93–100.

Bers, A. (1975). Linear waves and instabilities. In C. DeWitt & J. Peyraud (Eds.), *Physique des Plasmas*. Gordon & Breach. Chap. 4.

Briggs, R. J. (1964). *Electron-stream interaction with plasmas*. MIT Press. Chap. 2.

Clarke, D. B., Brandner, P. A., & Walker, G. J. (2007). Computational and experimental investigation of flow around a 3-1 Prolate spheroid. *AFMC*, 1381–1387.

Corke, T. C., & Knasiak, K. F. (1998). Stationary travelling cross-flow mode interactions on a rotating disk. *Journal of Fluid Mechanics, 355*, 285–315.

Faller, A. J. (1991). Instability and transition of disturbed flow over a rotating disk. *Journal of Fluid Mechanics, 230*, 245–270.

Garrett, S. J. (2002). The stability and transition of the boundary layer on rotating bodies (PhD thesis). Cambridge University.

Garrett, S. J. (2010a). Vortex-speed selection in the rotating-disk boundary layer. *Journal of Algorithms & Computational Technology, 4*(1).

Garrett, S. J. (2010b). Linear growth rates of type I & II convective modes within the rotating-cone boundary layer. *Fluid Dynamics Research, 42*, 025504.

Garrett, S. J. (2010c). Vortex-speed selection within the boundary-layer flow over a rotating sphere placed in an enforced axial flow. *European Journal of Mechanics B, 29*, 84–92.

Garrett, S. J. (2011). Vortex-speed selection within the transitional region of rotating boundary-layer flows. In *Proceedings of the 41st AIAA fluid dynamics conference*, Honolulu, HI, USA Paper AIAA-2011-3885.

Garrett, S. J., Hussain, Z., & Stephen, S. O. (2009). The crossflow instability of the boundary layer on a rotating cone. *Journal of Fluid Mechanics, 622*, 209–232.

Garrett, S. J., Hussain, Z., & Stephen, S. O. (2010). Boundary-layer transition on broad cones rotating in an imposed axial flow. *AIAA Journal, 48*, 2015–2027.

Garrett, S. J., & Peake, N. (2002). The stability and transition of the boundary layer on a rotating sphere. *Journal of Fluid Mechanics, 456*, 199–217.

Garrett, S. J., & Peake, N. (2004). The stability of the boundary layer on a rotating sphere in a uniform axial flow. *European Journal of Mechanics B, 23*, 241–253.

Garrett, S. J., & Peake, N. (2007). The absolute instability of the boundary layer on a rotating cone. *European Journal of Mechanics B, 26*, 344–353.

Gregory, N., Stuart, J. T., & Walker, W. S. (1955). On the stability of the three-dimensional boundary-layer with application to the flow due to a rotating disk. *Philosophical Transactions of the Royal Society A, 248*, 1955.

Hussain, Z., Stephen, S. O., & Garrett, S. J. (2011). The centrifugal instability of a slender rotating cone. *Journal of Algorithms & Computational Technology, 6*(1).

Hussain, Z., Garrett, S. J., & Stephen, S. O. (2011). The instability of the boundary layer over a disk rotating in an enforced axial flow. *Physics of Fluids, 23*, 1141108.

Kobayashi, R. & Arai, T. (1990). Spiral vortex behavior in transition region and separation of three-dimensional boundary layers on spheres rotating in axial flow. In Arnal, D. & Michel, R. (Ed.), *Laminar turbulent transition, IUTAM Symposium Toulouse*, (pp. 551–557). France.

Kobayashi, R., & Izumi, H. (1983). Boundary-layer transition on a rotating cone in still fluid. *Journal of Fluid Mechanics, 127*, 353–364.

Kobayashi, R., Kohama, Y., & Kurosawa, M. (1983). Boundary-layer transition on a rotating cone in axial flow. *Journal of Fluid Mechanics, 127*, 341–352.

Kohama, Y. (1985). Turbulent transition process of the spiral vortices appearing in the laminar boundary layer of a rotating cone. *Phys. Chem. Hydrodyn., 6*(5), 659.
Kohama, Y. P. (2000). Three-dimensional boundary layer transition study. *Current Science, 79*(6), 800–807.
Kohama, Y., & Kobayashi, R. (1983). Boundary-layer transition and the behavior of spiral vortices on rotating spheres. *Journal of Fluid Mechanics, 137*, 153–164.
Lingwood, R. J. (1995). Absolute instability of the boundary layer on a rotating disk. *Journal of Fluid Mechanics, 299*, 17–33.
Malik, M. R. (1986). The neutral curve for stationary disturbances in rotating-disk flow. *Journal of Fluid Mechanics, 164*, 275–287.
Manohar, R. (1967). The boundary on a rotating sphere. *Zeitschrift fur Angewandte Mathematik und Physik, 18*, 320.
Othman, H., & Corke, T. C. (2006). Experimental investigation of absolute instability of a rotating-disk boundary layer. *Journal of Fluid Mechanics, 565*, 63–94.
Owen, J. M., & Rogers, R. H. (1989). Flow and heat transfer in rotating-disc systems. Vol. 1 – Rotor-stator systems (Research Studies, Taunton, Sommerset, U.K).
Reed, H. L., & Saric, W. S. (1989). Stability of three-dimensional boundary layers. *Annual Review of Fluid Mechanics, 21*, 235.
Samad, A. (2010). The convective instability of the boundary-layer flow over families of rotating spheroids (PhD thesis). University of Leicester.
Samad, A., & Garrett, S. J. (2010). On the laminar boundary-layer flow over rotating spheroids. *International Journal of Engineering Science, 48*, 2015–2027.
Saric, W. S., Reed, H. L., & White, E. B. (2003). Stability and transition of three-dimensional boundary layers. *Annual Review of Fluid Mechanics, 35*, 413.
Sawatzki, O. (1970). Das Strömungsfeld un eine rotiernde kugel. *Acta Mechanica, 9*, 159–214.
Smith, N.H. (1947). Exploratory investigation of laminar-boundary-layer oscillations on a rotating disk, National Advisory Committee for aeronautics, Technical Note no. 1227, Washington DC, USA.
Taniguchi, H., Kobayashi, T., & Fukunishi, Y. (1998). Stability of the boundary layer on a sphere rotating in still fluid. *Acta Mechanica, 129*, 243–253.
Tezuka, A., & Suzuki, K. (2006). Three-dimensional global linear stability analysis of flow around a spheroid. *AIAA Journal, 48*(8).
Theodorsen, & Regier. (1945). Experiments on drag of revolving disks, cylinders and streamline rods at high speeds, National Advisory Committee for aeronautics, Report no. 793, Washington DC, USA.
Turkyilmazoglu, M., & Gajjar, J. S. B. (1998). Absolute and convective instability in the incompressible boundary layer on a rotating disk. Report no. CLSCM, University of Manchester.
Van Dyke, M. (1982). *Album of fluid motion*. Stanford, California: Parabolic Press.
Wimmer, M. (1988). Viscous flows and instabilities near rotating bodies. *Progress in Aerospace Sciences, 25*, 43.